Nano Research

Open Access

Research Article

Defect-rich $Mg(OH)_2$ nanosheets as high-performance antioxidants

Ziyang Liu[1,§], Xiang Yang[1,§], Xulin Zhou[1], Yiping Ning[1], Bingqing Wang[1], Aijuan Han[1], Yanjun Lin[2,3] ✉, Junfeng Liu[1] ✉, and Xue Duan[1,3]

[1] *State Key Laboratory of Chemical Resource Engineering, Beijing University of Chemical Technology, Beijing 100029, China*
[2] *Salt Lake Chemical Engineering Research Complex, Qinghai Provincial Key Laboratory of Salt Lake Materials Chemical Engineering, Qinghai University, Xining 810016, China*
[3] *Quzhou Institute for Innovation in Resource Chemical Engineering, Quzhou 324000, China*
[§] *Ziyang Liu and Xiang Yang contributed equally to this work.*

Cite this article: *Nano Research*, **2026**, *19*, 94908409. https://doi.org/10.26599/NR.2026.94908409

ABSTRACT: The development of highly efficient radical scavengers remains a substantial challenge in materials chemistry. Here, we report defect-rich $Mg(OH)_2$ nanosheets (d-$Mg(OH)_2$), synthesized via rapid nucleation within a colloid mill, as a potent multifunctional antioxidant. Compared to commercial $Mg(OH)_2$ (c-$Mg(OH)_2$), d-$Mg(OH)_2$ demonstrates markedly superior scavenging capabilities against a broad spectrum of radicals, including $\cdot O_2^-$, ·OH, ·NO, DPPH·, and ·Cl. Mechanistic investigations and density functional theory calculations reveal a dual-mode scavenging mechanism: hydrogen atom transfer for ·OH, ·NO, and ·Cl, and electron transfer for $\cdot O_2^-$ and DPPH·, with significantly reduced energy barriers on the defect-rich surface. We further demonstrate the material's practical efficacy in scavenging intracellular reactive oxygen species and enhancing the thermal stability of polyvinyl chloride. This work establishes a defect-engineering approach to activate earth-abundant hydroxides as high-performance antioxidants, with promising applications in biomedicine and polymer stabilization.

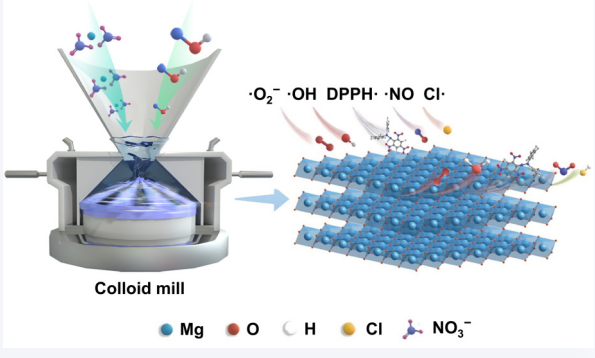

KEYWORDS: $Mg(OH)_2$, free radical, scavenger, oxygen defect, antioxidant

1 Introduction

Free radicals are extremely reactive substances characterized by unpaired electrons, making them highly unstable and causing harmful consequences in a variety of fields, including biology, food science, and materials chemistry [1–4]. These radicals can attack biologically relevant molecules and cause oxidative stress damage, resulting in inflammation and even cell degeneration and apoptosis [5]. Moreover, research has revealed that the undesired polymer degradation under light, heat, or ozone mainly occurs through a chain reaction process driven by free radicals [6]. For example, when exposed to elevated temperature or ultraviolet radiation, thermally unstable structures in polyvinyl chloride (PVC), such as allyl chloride groups, undergo decomposition and generate chlorine radicals (·Cl), which leads to severe discoloration and a notable decrease in performance [7]. Although small molecular organic antioxidants or enzymes exhibit effective radical scavenging capabilities, they are often plagued by issues such as low stability, high cost, and challenging storage conditions [8, 9]. Nano-antioxidants, i.e., nanoparticles possessing intrinsic antioxidant features, have recently aroused increasing interest because of their high efficiency and durable stability, relatively large surface area, and controllable synthesis, which opens up new avenues for free radical scavenging [2, 10–12].

In recent years, $Mg(OH)_2$ has gained attention for its unique physical and chemical properties, finding applications across various fields such as biomedical science [13, 14], wastewater treatment [15], and flame retardant [16]. Notably, surface defects were demonstrated to play an important role in enhancing the performance of nanomaterials [17–24]. In the case of $Mg(OH)_2$ nanomaterials, Lin et al. studied the influence of surface defects on the adsorption capacity of toxic heavy metal oxyanions in $Mg(OH)_2$ nanosheets, revealing that heavy metal oxyanions can be stably incorporated into surface defects [25]. Fan et al. found that an

Received: November 28, 2025; **Revised:** January 4, 2026
Accepted: January 5, 2026

✉Address correspondence to Junfeng Liu, ljf@mail.buct.edu.cn; Yanjun Lin, linyj@mail.buct.edu.cn

increase in hydroxyl defects on the $Mg(OH)_2$ support led to an enhanced O_2 activation of Au/$Mg(OH)_2$ [26]. Although $Mg(OH)_2$ has not yet been developed as an antioxidant, the integration of defect engineering into $Mg(OH)_2$ nanomaterials holds promising potential in terms of unveiling new possibilities.

Herein, we present a strategy based on defect-rich induced activation of inert $Mg(OH)_2$ for the efficient scavenging of various radicals. X-ray absorption spectroscopy (XAS) analysis reveals that, compared with commercial $Mg(OH)_2$ (c-$Mg(OH)_2$), the defect-rich $Mg(OH)_2$ (d-$Mg(OH)_2$) synthesized via the nucleation and crystallization method in a colloid mill contains abundant oxygen and metal defects. In various free radical scavenging experiments (including $\cdot O_2^-$, ·OH, ·NO, DPPH·, and ·Cl), the prepared d-$Mg(OH)_2$ demonstrated remarkable free radical scavenging capacity. Mechanistic studies have demonstrated that d-$Mg(OH)_2$ scavenges free radicals by employing two distinct pathways: a hydrogen atom transfer mechanism for ·OH, ·NO, and ·Cl, and an electron transfer mechanism for $\cdot O_2^-$ and DPPH·. Density functional theory (DFT) calculations demonstrate that the superior free radical scavenging activity of d-$Mg(OH)_2$ is attributed to a substantial reduction in the energy barriers associated with both the hydrogen transfer and electron transfer mechanisms, and Bader charge analysis confirms the validity of these two mechanisms. More importantly, the prepared d-$Mg(OH)_2$ demonstrates excellent application potential in both biological and materials science fields: it can efficiently scavenge intracellular reactive oxygen species (ROS), significantly alleviating oxidative damage induced by Rosup; meanwhile, in polymer systems, it effectively enhances the thermal stability of polyvinyl chloride (PVC) and inhibits its thermal decomposition process. This research opens new avenues for the prospective application of $Mg(OH)_2$ as a promising antioxidant in the field of materials chemistry while highlighting the defect effects of nanomaterials for free radical scavenging.

2 Experiment section

2.1 Synthesis of d-$Mg(OH)_2$

d-$Mg(OH)_2$ nanosheets were synthesized by the rapid nucleation method in a colloid mill. Typically, 120 mL of 0.156 M $Mg(NO_3)_2{\cdot}6H_2O$ and 0.313 M NaOH were added to the colloid mill nucleation reactor using a peristaltic pump, and the solution was mixed rapidly for 1 min at a speed of 3000 rpm. The supernatant of the resulting dispersion was then removed by centrifugation, and the precipitate was washed with deionized water and ethanol twice.

2.2 $\cdot O_2^-$ scavenging activity assay

The production of $\cdot O_2^-$ involved dissolving KO_2 in anhydrous DMSO with the aid of co-solvent 18-crown-6. Nitro blue tetrazolium chloride (NBT) with an absorbance peak at 680 nm was used to detect $\cdot O_2^-$, which can produce formazan upon the reaction of $\cdot O_2^-$ [27]. Typically, 0.09 g 18-crown-6 and 7.8 mg KO_2 were added to 20 mL anhydrous DMSO to produce an $\cdot O_2^-$ solution. 6 mg NBT was quickly added to 45 mL of anhydrous DMSO to obtain the NBT solution. Then, 20 mg scavengers were added quickly to 6 mL $\cdot O_2^-$ solution in a brown glass bottle and stirred for 10 min. 0.1 mL of reaction supernatant was extracted and reacted with 7 mL of NBT chromogenic solution in the dark for 10 min, and its absorbance at 680 nm was measured. The reaction was maintained at about 20 °C under argon protection throughout the experiment.

2.3 ·OH scavenging activity assay

The ·OH scavenging activity test involved the generation of ·OH by Fenton reaction and the detection by terephthalic acid (TA), which forms 2-hydroxyterephthalic acid when reacting with ·OH with a fluorescent peak at 425 nm [28, 29]. Typically, 12 mg of scavengers were added to the solution containing 1.25 mL of 6 mM H_2O_2 and 1.25 mL of 15 μM $FeSO_4{\cdot}7H_2O$ to react for 45 min. Then, 0.5 mL TA solution (30 mM) was incorporated into the mixture and stirred for 30 min. The supernatant was collected by centrifugation for the fluorescence test.

2.4 DPPH· scavenging activity assay

DPPH·, a dark purple crystalline powder, exhibits a strong ultraviolet–visible (UV–Vis) absorption peak at 518 nm in its solution. In the presence of antioxidants, the color of the solution gradually shifts from deep purple to light yellow, indicating the scavenging of DPPH· [30]. The efficiency of the material can be determined by the change in peak absorbance at 518 nm, where lower absorbance indicates better DPPH· scavenging performance. In a typical experiment, 6.3 mg of DPPH· was dissolved in 4 mL of CCl_4 to prepare a DPPH· solution. Subsequently, 40 mg of scavengers were added into a brown vial containing 6 mL of CCl_4 and evenly dispersed. Thereafter, 150 μL of the above DPPH· solution was added. After 2 h, the supernatant was collected by centrifugation for UV analysis.

2.5 ·NO scavenging activity assay

The ·NO scavenging activity test involved the generation of ·NO by sodium nitroprusside (SNP) in pH buffer solution. The ·NO reacts with oxygen in solution to form nitrite ions, which can be detected using Griess reagent, producing a characteristic UV–Vis absorption change at 510 nm. In a typical experiment, 4 mg of SNP was dissolved in 3 mL of phosphate buffer (pH = 7.4) by ultrasonication. Then 12 mg of scavenger powder was added to the solution and allowed to react for 150 min. Following centrifugation, 0.2 mL of Griess reagent was mixed with 0.8 mL of the reaction mixture and reacted for 2 min. Finally, the absorbance of the solution was recorded.

2.6 ·Cl scavenging activity assay

·Cl is generated by photocatalytic decomposition of BiOCl, and detected by methylene blue (MB) as a probe [31, 32]. Typically, 30 mg of BiOCl was dispersed in 5 mL of NaOH solution (pH = 10), followed by a 3-minute xenon light irradiation to produce ·Cl. Then, 30 mg of scavengers were added to the reaction system, followed by the addition of 50 μL of 60 mM MB, and reacted for 2 min. Finally, the supernatant was collected by centrifugation for UV–Vis analysis.

2.7 Cell viability assay

Intracellular ROS was detected using 2',7'-dichlorofluorescein diacetate (DCFH-DA), a nonfluorescent compound that reacts with intracellular ROS to produce the fluorescent product dichlorofluorescein (DCF). Specifically, Mouse macrophages (RAW264.7 cells) were seeded in a 6-well plate and cultured for 24 h. Then, the cells were treated with 20 μg/mL of various $Mg(OH)_2$ and incubated for 12 h at 37 °C. Oxidative stress was then induced by exposing the cells to Rosup (50 μg/mL) for 12 h. Following this, a 10 μM DCFH-DA solution was added to the RAW264.7 cells, and the mixture was incubated for another 12, 24,

and 48 h. After unloading the DCFH-DA by washing with PBS, the fluorescence intensity of cells was monitored by flow cytometry and fluorescence microscopy.

2.8 Static thermal aging test

30 g PVC powder, 12 g di-n-octyl phthalate (DNOP), 0.4 g zinc stearate ($Zn(st)_2$), 0.72 g calcium stearate ($Ca(st)_2$), and 0.6 g $Mg(OH)_2$ samples were blended in a double-roller mixer for 5 min at 140 °C. The blended material was subsequently compression molded into a 1 mm thick film at 140 °C and then cut into strips measuring 1.5 cm × 1.5 cm. These strips were placed in a thermal aging test box (JZ401A) and exposed to a temperature of 180 °C. At 10-minute intervals, the strips were removed and examined for color changes.

3 Results and discussion

3.1 Synthesis and characterization of d-$Mg(OH)_2$

Ultrathin d-$Mg(OH)_2$ nanosheets were prepared by a rapid collisional nucleation process in saline and alkaline solutions in a colloid mill, as shown in Fig. 1(a). This process prevents nuclei from agglomerating and crystallizing, resulting in the synthesis of d-$Mg(OH)_2$ with an abundance of defects. Transmission electron microscope (TEM) images reveal that the synthesized d-$Mg(OH)_2$ has a sheet-like structure with an average size of approximately 60 nm (Fig. 1(b)). Compared with the commercial $Mg(OH)_2$ (c-$Mg(OH)_2$, Fig. S1(a) in the Electronic Supplementary Material (ESM)), d-$Mg(OH)_2$ nanosheets exhibit a smaller particle size due to the quick nucleation process in the colloid mill. Moreover, the high-resolution TEM (HRTEM) image of d-$Mg(OH)_2$ nanosheets showed a lattice fringe spacing of 0.23 nm, which corresponds to the (101) facet of $Mg(OH)_2$ (inset in Fig. 1(c)). The thickness of d-$Mg(OH)_2$ nanosheets was further analysed through atomic force microscope (AFM), which is approximately 5 nm as shown in Fig. S2 in the ESM. Additionally, the crystal structure of d-$Mg(OH)_2$ nanosheets is characterized by XRD (Fig. 1(d)). The diffraction peaks of d-$Mg(OH)_2$ align well with the standard $Mg(OH)_2$ (JCPDS No. 44-1482), and no additional diffraction peaks indicate the presence of impurities. Compared to c-$Mg(OH)_2$, d-$Mg(OH)_2$ exhibits weaker XRD peak intensity, indicating lower crystallinity and smaller particle size.

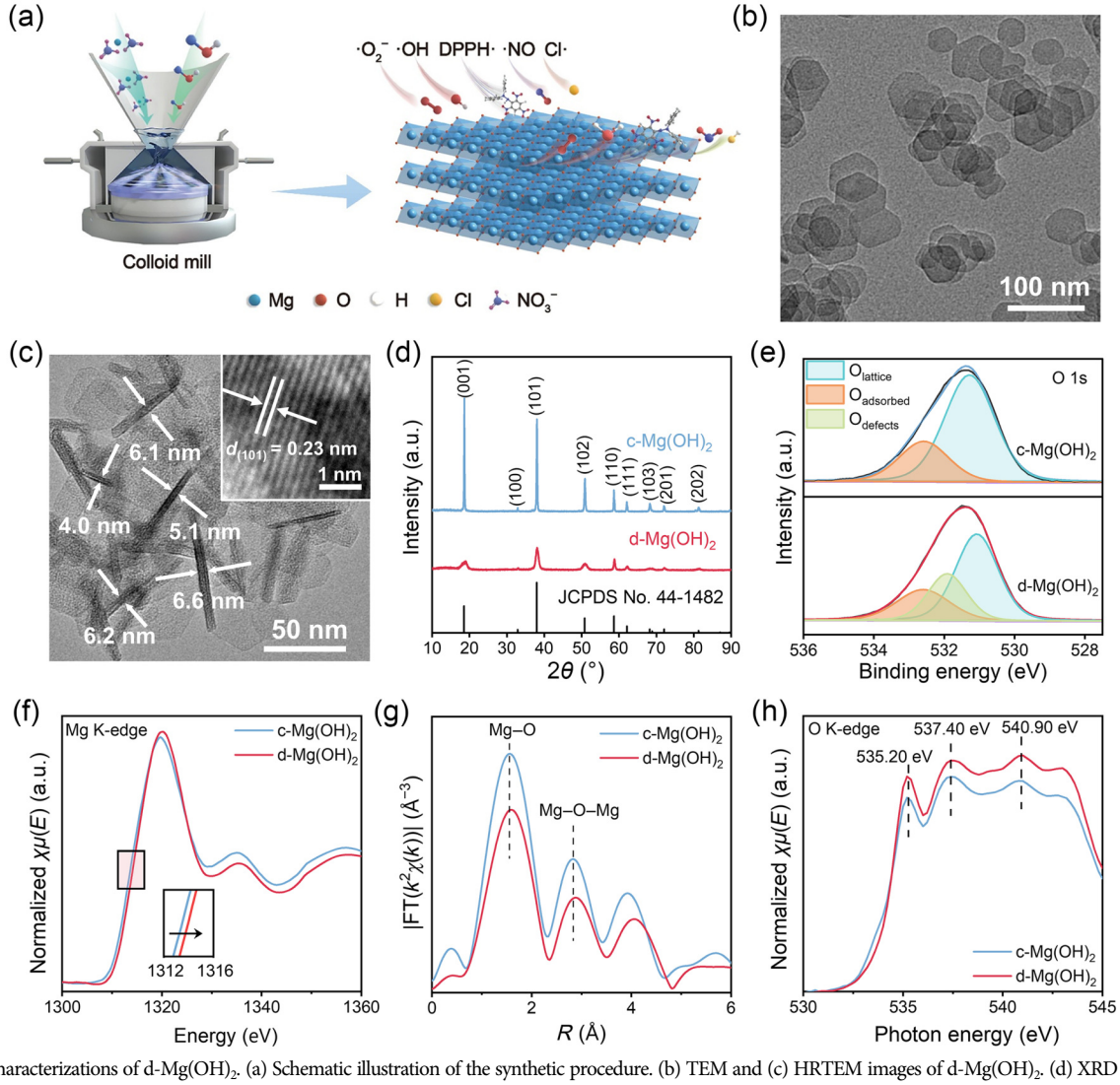

Figure 1 Characterizations of d-$Mg(OH)_2$. (a) Schematic illustration of the synthetic procedure. (b) TEM and (c) HRTEM images of d-$Mg(OH)_2$. (d) XRD patterns and (e) XPS spectra of O 1s of d-$Mg(OH)_2$ and c-$Mg(OH)_2$. (f) XANES Mg K-edge, (g) corresponding k^2-weighted Fourier transform (FT) spectra, and (h) XANES O K-edge of d-$Mg(OH)_2$ compared to c-$Mg(OH)_2$.

X-ray photoelectron spectroscopy (XPS) was performed to investigate the surface properties of d-$Mg(OH)_2$. As shown in Fig. 1(e), the XPS O 1s peak of c-$Mg(OH)_2$ can be deconvoluted into two distinct peaks, with one peak at 531.1 eV attributed to lattice oxygen and another at 532.6 eV corresponding to surface-adsorbed oxygen. In contrast, an additional peak at 531.9 eV appeared in d-$Mg(OH)_2$, which is associated with oxygen defects [33]. Furthermore, compared with c-$Mg(OH)_2$, the Mg 2p binding energy in d-$Mg(OH)_2$ exhibits a notable shift toward higher values (Fig. S3 in the ESM), indicating a higher oxidation state and reduced electron density of Mg relative to c-$Mg(OH)_2$, which is consistent with the presence of oxygen defects.

X-ray absorption near-edge structure (XANES) measurements were used to further elucidate the chemical environment of $Mg(OH)_2$. Figure 1(f) shows the Mg K-edge XANES spectrum of d-$Mg(OH)_2$, in which the absorption edge shifts towards higher energy compared to c-$Mg(OH)_2$, indicating that Mg has a higher oxidation state in d-$Mg(OH)_2$ [34], consistent with the XPS result of Mg in Fig. S3 in the ESM. Fourier transform extended X-ray absorption fine structure (FT-EXAFS) analysis further reveals that two coordination shell peaks are present in both d-$Mg(OH)_2$ and c-$Mg(OH)_2$, located at 1.55 and 2.82 Å, respectively, corresponding to Mg–O and Mg–O–Mg bonds (Fig. 1(g)). However, the peak intensities in the d-$Mg(OH)_2$ sample are significantly lower than those in the c-$Mg(OH)_2$ sample, indicating a reduced coordination number. EXAFS fitting was performed to obtain quantitative structural information on the Mg atoms (Fig. S4 and Table S1 in the ESM). The coordination numbers of Mg–O and Mg–O–Mg in the c-$Mg(OH)_2$ sample were both close to 6, consistent with the theoretical values expected for a perfect $Mg(OH)_2$ crystal. In contrast, the coordination numbers of Mg–O and Mg–O–Mg in the d-$Mg(OH)_2$ sample were significantly lower, indicating the presence of oxygen and metal defects in the surface lattice. In addition, the intensity of the O K-edge in d-$Mg(OH)_2$ increased compared to c-$Mg(OH)_2$, which could be ascribed to a large number of defects of the local structure in d-$Mg(OH)_2$ (Fig. 1(h)) [35]. The Mg content in d-$Mg(OH)_2$ was measured by inductively coupled plasma (ICP) and was found to be 39.86%, showing a reduction of approximately 1.38% relative to c-$Mg(OH)_2$ (Table S2 in the ESM), consistent with the presence of metal defects. Furthermore, the electron paramagnetic resonance (EPR) spectrum of d-$Mg(OH)_2$ exhibits a strong signal at g = 2.000 (Fig. S5 in the ESM), indicating a higher concentration of oxygen defects [36], consistent with XPS O 1s analysis. In addition, nitrogen adsorption-desorption isotherms indicate that d-$Mg(OH)_2$ exhibits a larger specific surface area (145.98 m^2/g, Table S3 in the ESM) due to its smaller nanosheet size and abundant defects, thereby exposing more active sites.

3.2 Multiple radical scavenging activities and mechanisms of d-$Mg(OH)_2$

3.2.1 $\cdot O_2^-$ scavenging activity and mechanism of d-$Mg(OH)_2$

The scavenging activity of d-$Mg(OH)_2$ towards $\cdot O_2^-$ was investigated using the KO_2-NBT system, and the results are shown in Fig. 2(a) [37]. In the absence of a scavenger, the highest level of $\cdot O_2^-$ was indicated by the absorbance at 680 nm. The addition of d-$Mg(OH)_2$ significantly reduced the absorbance at 680 nm, achieving a $\cdot O_2^-$ clearance rate of 75%, which notably surpassed that of c-$Mg(OH)_2$, confirming the importance of defects in its activity to scavenge $\cdot O_2^-$.

To elucidate the scavenging mechanism of d-$Mg(OH)_2$ for $\cdot O_2^-$ radicals, we analyzed the electron transfer process by examining the changes in the chemical states of magnesium and oxygen in d-$Mg(OH)_2$ before and after the reaction. In the Mg K-edge XANES spectrum (Fig. 2(b)), the absorption edge shifted toward lower energy after the reaction of d-$Mg(OH)_2$ with $\cdot O_2^-$, indicating reduction of Mg. This finding is corroborated by XPS analysis (Fig. 2(c)), which showed a decrease in the binding energy of the Mg 2p peak, suggesting electron transfer to Mg. In contrast, the O 1s peak (Fig. S4(a) in the ESM) remained largely unchanged. These results indicate that the scavenging of $\cdot O_2^-$ by d-$Mg(OH)_2$ occurs via an electron transfer mechanism. Following the scavenging reaction, electrons from the $\cdot O_2^-$ are transferred to the magnesium atoms in d-$Mg(OH)_2$, leading to the generation and release of oxygen within the system, as evidenced by the bubble formation observed during the reaction process.

3.2.2 ·OH scavenging activity and mechanism of d-$Mg(OH)_2$

By using TA as a probe, the fluorescence peak intensity of ·OH produced by the Fenton reaction at 425 nm was detected, and the scavenging ability of d-$Mg(OH)_2$ towards ·OH was studied. As shown in Fig. 2(d), the addition of d-$Mg(OH)_2$ led to a substantial decrease in the fluorescence signal peaks, indicating its remarkable capability to scavenge ·OH, surpassing that of c-$Mg(OH)_2$. Likewise, XANES and XPS analyses were conducted to determine the chemical state changes of Mg and O before and after the scavenging reaction. As shown in Fig. 2(e), the Mg K-edge absorption edge of d-$Mg(OH)_2$ shifted toward higher energy after the ·OH scavenging reaction, indicating a loss of electrons from Mg during the process. Furthermore, both the Mg and O XPS spectra exhibited shifts to higher binding energy (Fig. 2(f) and Fig. S4(b) in the ESM), confirming a reduction in electron density for both elements. These electronic structure changes are consistent with a hydrogen atom transfer mechanism, in which ·OH radicals combine with hydrogen atoms from surface hydroxyl groups and desorb as water molecules, leading to the observed changes in the apparent electronic states of magnesium and oxygen.

3.2.3 DPPH· scavenging activity and mechanism of d-$Mg(OH)_2$

The scavenging ability of d-$Mg(OH)_2$ towards nitrogen-centered radicals was first investigated by examining the scavenging properties on DPPH·. Notably, d-$Mg(OH)_2$ exhibited a significantly higher scavenging rate of 80% compared to c-$Mg(OH)_2$, which demonstrated negligible scavenging activity (Fig. 2(g)). In addition, the Mg K-edge XANES spectrum reveals a higher oxidation state of Mg in d-$Mg(OH)_2$ after the reaction (Fig. S7(a) in the ESM). The comparison of the peak position in the XPS results (Figs. S7(b) and S7(c) in the ESM) reveals a distinct shift towards higher binding energy for both the Mg 2p and O 1s peaks after radical scavenging reactions, indicating electron loss from both Mg and O. This electronic structure change is consistent with the DPPH· scavenging mechanism observed in MgAl-layered double hydroxides, indicating that both systems follow an electron transfer pathway [11]. Specifically, d-$Mg(OH)_2$ achieves scavenging through the donation of electrons to DPPH·.

3.2.4 ·NO scavenging activity and mechanism of d-$Mg(OH)_2$

The scavenging activity of d-$Mg(OH)_2$ on ·NO was investigated using the Griess reagent as a probe. As shown in Fig. 2(h), the presence of ·NO in the solution resulted in a strong absorption at

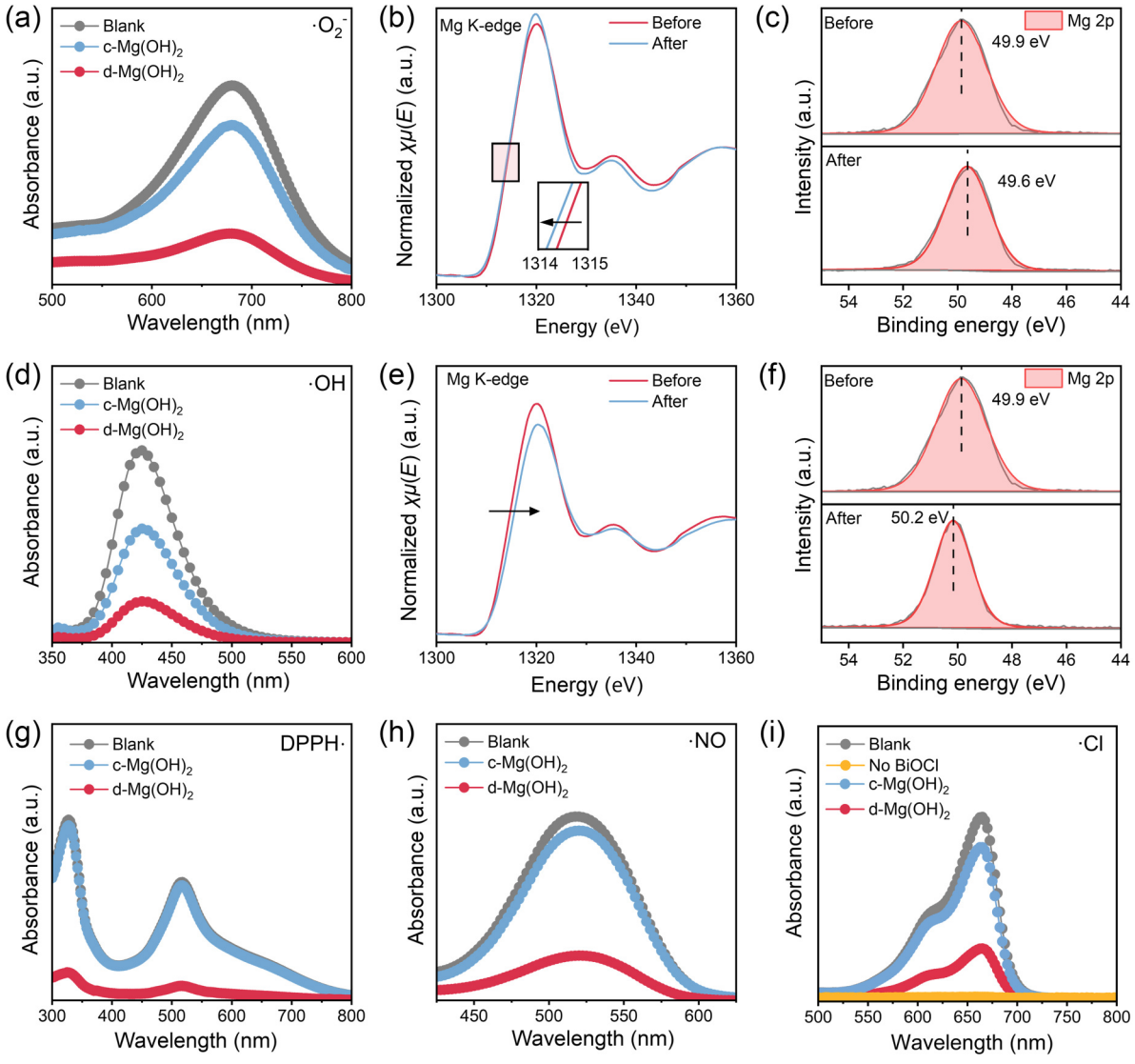

Figure 2 Multiple radical scavenging activities of $Mg(OH)_2$. (a) UV–Vis absorbance spectra, (b) Mg K-edge XANES, and (c) XPS Mg 2p before and after $\cdot O_2^-$ scavenging reaction. (d) FL spectra, (e) Mg K-edge XANES, and (f) XPS Mg 2p before and after the ·OH scavenging reaction. UV–Vis absorbance spectra of (g) DPPH·, (h) ·NO, and (i) ·Cl scavenging reaction.

510 nm. Upon the addition of d-$Mg(OH)_2$ to this solution, a significant decrease in absorption was observed, suggesting that d-$Mg(OH)_2$ effectively scavenged ·NO.

In addition, d-$Mg(OH)_2$ exhibited substantially enhanced scavenging activity towards ·NO when compared to c-$Mg(OH)_2$. To investigate how d-$Mg(OH)_2$ scavenges ·NO, changes in the chemical states of Mg and O before and after the reaction were analyzed. The Mg K-edge XANES spectrum reveals a higher oxidation state of Mg in d-$Mg(OH)_2$ after the reaction (Fig. S7(d) in the ESM). XPS results of d-$Mg(OH)_2$ demonstrate that the Mg 2p and O 1s spectra shift towards high binding energy after the reaction, confirming a reduction in the electron density around Mg atoms (Figs. S7(e) and S7(f) in the ESM), which was consistent with the Mg K-edge data. This corresponds to the electronic structure changes observed in the ·OH scavenging experiment, confirming that hydrogen atom transfer occurred during the ·NO radical scavenging process, resulting in the alteration of the electronic environment of the magnesium and oxygen centers and the formation of HNO, which ultimately decomposes into N_2O and OH^- [38].

3.2.5 *·Cl scavenging activity and mechanism of d-$Mg(OH)_2$*

The ability of d-$Mg(OH)_2$ to scavenge ·Cl was verified by the methylene blue (MB) degradation experiment, as shown in Fig. 2(i). While MB faded rapidly after photo-catalytically generating ·Cl, the addition of d-$Mg(OH)_2$ dramatically prevented such degradation, as evidenced by strong absorbance around 665 nm, indicating its remarkable ·Cl scavenging activity. In contrast, c-$Mg(OH)_2$ exhibited inferior performance in terms of scavenging capability. The mechanism of d-$Mg(OH)_2$ scavenging ·Cl was also investigated. As shown in Figs. S7(g) and S7(h) in the ESM, both the Mg K-edge absorption edge and the XPS Mg 2p peak of d-$Mg(OH)_2$ shifted to high binding energy after the reaction, indicating the electron depletion of Mg. Similarly, the XPS O 1s spectrum also displayed a high binding energy shift after the reaction, suggesting the electron loss from O atoms (Fig. S7(i) in the ESM). These results are in excellent agreement with the hydrogen transfer process, in which the reaction proceeds by extracting

hydrogen atoms from d-$Mg(OH)_2$ to form HCl.

3.3 DFT studies on free radical scavenging activity of d-$Mg(OH)_2$

To further understand the origins of the remarkable radical scavenging performance exhibited by the d-$Mg(OH)_2$, DFT calculations were employed to investigate the underlying mechanism. Two $Mg(OH)_2$ models, one incorporating metal vacancy (Mv) and oxygen vacancy (Ov) (Fig. 3(a)), and the other without such defects, were constructed to represent d-$Mg(OH)_2$ and c-$Mg(OH)_2$, respectively. Bader charge analysis indicates significant charge redistribution upon the introduction of defects. For d-$Mg(OH)_2$, the Mg sites lose more charge (average −1.29 e) than in the intact structure (c-$Mg(OH)_2$, average −1.26 e), rendering them more Lewis acidic and thereby enabling stronger coordination with oxygen or nitrogen-containing radicals. At the same time, the enhanced positive charge on the Mg sites strengthens the electrostatic attraction with negatively charged superoxide radicals, collectively boosting their adsorption energy. The corresponding free-energy profiles for the different radical scavenging reactions on d-$Mg(OH)_2$ and c-$Mg(OH)_2$ are illustrated in Figs. 3(b)–3(f). As shown in Fig. 3(b), the spontaneous adsorption of ·OH on d-$Mg(OH)_2$ reduces the free energy barrier of the rate-determining step from 2.48 to 1.45 eV compared to c-$Mg(OH)_2$, which significantly enhances the effectiveness of ·OH scavenging. Similar mechanisms are observed for $\cdot O_2^-$, ·NO, and ·Cl (Figs. 3(b) and 3(c)). Furthermore, in the case of DPPH·, the free energy associated with the rate-determining step decreases from 0.80 to 0.33 eV. The ·DPPH radical is converted into $DPPH^-$ following the acquisition of an e^- from d-$Mg(OH)_2$. A similar clear reaction pathway is also observed for $\cdot O_2^-$ (Figs. 3(d) and 3(e)). The DFT analysis demonstrates that the free energy barriers for the rate-determining steps of various free radical scavenging processes are substantially lower on d-$Mg(OH)_2$ than on c-$Mg(OH)_2$ (Figs. 3(b)–3(f)), providing a mechanistic explanation for the significantly enhanced scavenging activity of d-$Mg(OH)_2$ toward multiple free radicals. In addition, the electronic structure changes of d-$Mg(OH)_2$ following the removal of free radicals via hydrogen atom transfer and electron transfer mechanisms were simulated using Bader charge analysis (Table S4 in the ESM). Specifically, the electron distribution of d-$Mg(OH)_2$ after scavenging ·OH, ·NO, and ·Cl radicals was simulated by removing a surface H atom from the OH group in d-$Mg(OH)_2$. For the electron distribution of d-$Mg(OH)_2$ following the removal of $\cdot O_2^-$ and DPPH·, an additional electron was introduced into, or one electron was removed from, d-$Mg(OH)_2$, respectively, to simulate the corresponding states. The calculation results are presented in Table S4 in the ESM. Following hydrogen atom transfer, both Mg and O atoms lose electrons. Similarly, after the removal of one electron via the electron transfer mechanism, both Mg and O atoms lose electrons as well. In contrast, when additional electrons are introduced, both Mg and O atoms gain electrons, which is consistent with the results observed by XPS and XANES.

3.4 Intracellular ROS scavenging activities of d-$Mg(OH)_2$

Given the high radical scavenging activity of d-$Mg(OH)_2$, we subsequently examined its intracellular antioxidative activities. Oxidative stress was stimulated by Rosup, and 2',7'-dichlorofluorescein diacetate (DCFH-DA) was utilized as the fluorescence probe to quantify the intracellular ROS levels. As shown in Fig. 4(a), high fluorescence signals were detected in RAW264.7 cells under Rosup stimulation for 12 h. When d-$Mg(OH)_2$ and c-$Mg(OH)_2$ were added, the fluorescence intensity decreased. Notably, d-$Mg(OH)_2$ caused a dramatic reduction in fluorescence signals. Flow cytometry quantitative analysis revealed that nearly 87.1 % of ROS could be eliminated (Figs. 4(b) and 4(c)). With the incubation time increasing to 24 h and 48 h, d-$Mg(OH)_2$ demonstrated sustained intracellular ROS scavenging activity, with

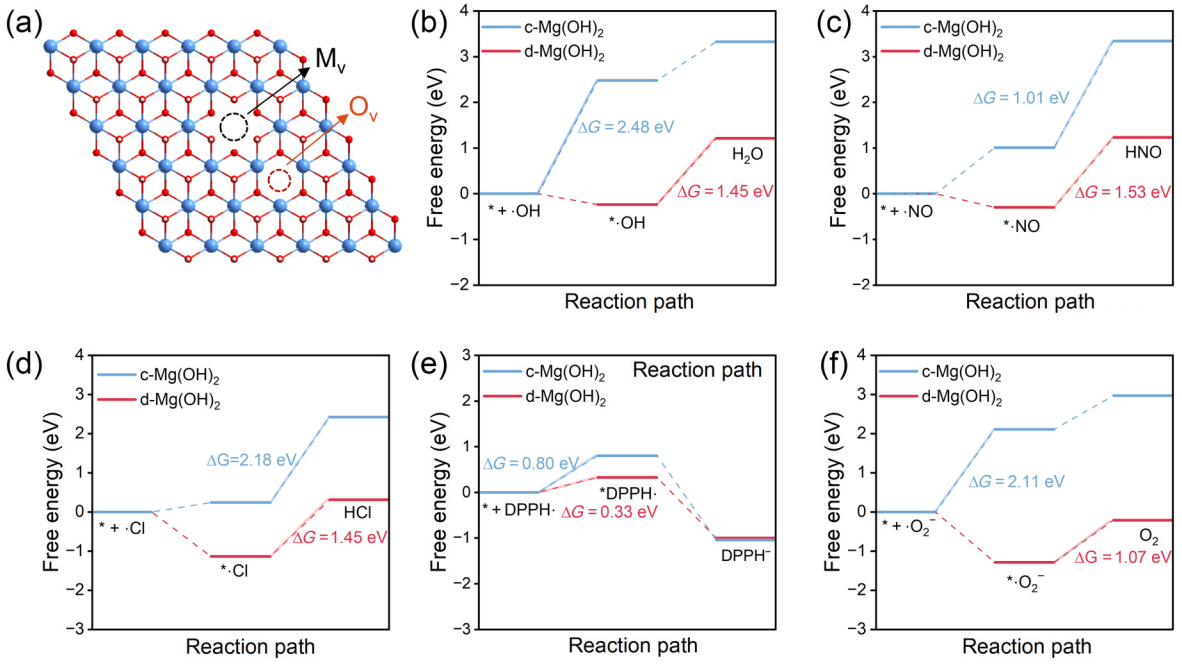

Figure 3 DFT studies of the free radical scavenging mechanism on d-$Mg(OH)_2$ compared with that on c-$Mg(OH)_2$. (a) Schematic illustration of d-$Mg(OH)_2$ structure, showing the presence of metal vacancies (Mv) and oxygen vacancies (Ov). The blue, red, and white spheres represent Mg, O, and H atoms, respectively. Free energy diagrams for the scavenging of (b) ·OH, (c) ·NO, (d) ·Cl, (e) DPPH· and (f) $\cdot O_2^-$.

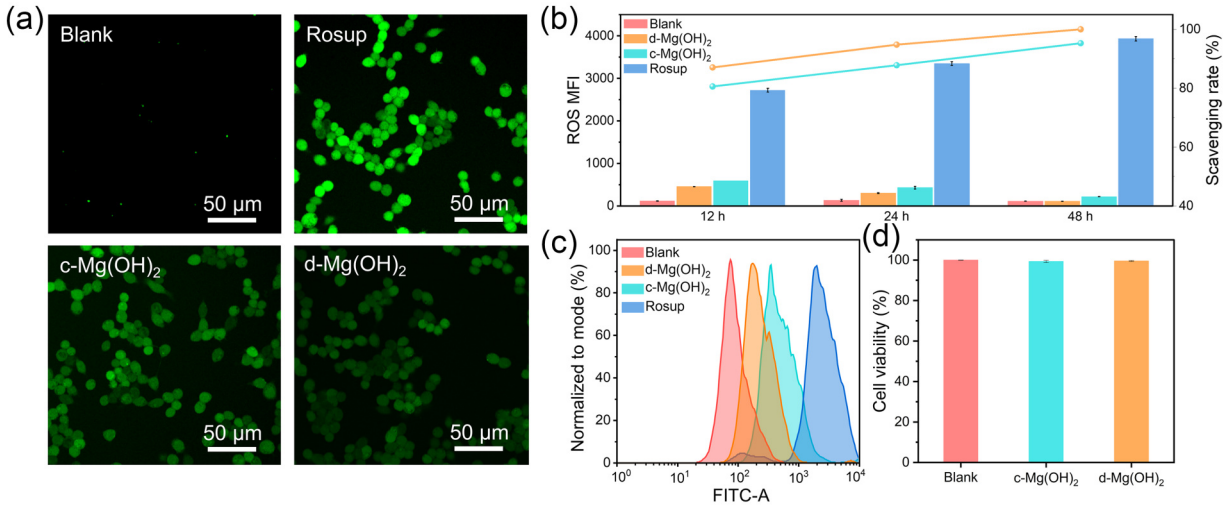

Figure 4 Cytoprotective ability of the d-$Mg(OH)_2$. (a) Detection of ROS-scavenging ability of d-$Mg(OH)_2$ and c-$Mg(OH)_2$ in RAW264.7 cells under Rosup stimulations for 12 h by fluorescence microscopy. (b) Time-dependent intracellular antioxidative activities and intracellular mean fluorescence intensity (MFI) of d-$Mg(OH)_2$ and c-$Mg(OH)_2$ in RAW264.7 cells under Rosup stimulations. (c) Normalized flow cytometric analysis of intracellular ROS under Rosup stimulation for 12 h. (d) Cell viability of RAW264.7 cells after incubation with d-$Mg(OH)_2$ and c-$Mg(OH)_2$ for 12 h.

the scavenging efficiency progressively increasing over time (Fig. 4(b)). At 48 h, d-$Mg(OH)_2$ was capable of scavenging 100% of ROS, highlighting its remarkable stability under these conditions. These findings suggest that d-$Mg(OH)_2$ can effectively and continuously scavenge intracellular ROS. In addition, the biocompatibility of the nanozyme is also investigated. As shown in Fig. 4(d), after incubating RAW264.7 cells with d-$Mg(OH)_2$ for 12 h at 37 °C, no significant alteration in cell viability was observed, indicating the excellent biocompatibility and biosafety of d-$Mg(OH)_2$.

3.5 Thermal stability test

Chlorine radical plays a critical role in the aging and degradation of polymers such as polyvinyl chloride (PVC) due to its strong oxidizing properties [39]. Inspired by the highly efficient chlorine radical scavenging capability of d-$Mg(OH)_2$, this material demonstrates significant potential in suppressing polymer degradation and enhancing thermal stability. Accordingly, this study further investigates the thermal stabilizing effect of d-$Mg(OH)_2$ on PVC. The PVC composite was cut into 1.5 cm × 1.5 cm strips and subjected to static thermal aging at 180 ± 1 °C in the thermal aging test box, where color changes in the sample were recorded. The thermal stability time of PVC was determined by the appearance of black decomposition. As shown in Fig. 5(a), the resistance of PVC to coloring lasted for approximately 50 min in the absence of $Mg(OH)_2$. However, the introduction of c-$Mg(OH)_2$ significantly enhanced the thermal stability of PVC, resulting in an extended duration of 60 min before discoloration occurred (Fig. 5(b)). Notably, the addition of d-$Mg(OH)_2$ exhibited a remarkable improvement in the thermal stability of PVC, leading to a prolonged stabilization time of 110 min as illustrated in Fig. 5(c). This finding suggests that d-$Mg(OH)_2$ effectively mitigates the decomposition process of PVC.

4 Conclusion

In conclusion, through a synthetic route involving rapid nucleation in a colloid mill, we successfully synthesized d-$Mg(OH)_2$, which demonstrates superior scavenging performance against a variety of free radicals. The combined experimental and theoretical study elucidates the mechanism by which d-$Mg(OH)_2$ scavenges free radicals: hydrogen atom transfer to ·OH, ·NO, and ·Cl, and electron transfer to $\cdot O_2^-$ and DPPH·. Both processes exhibit significantly enhanced activity due to the defect structure, which substantially lowers the reaction energy barrier. Finally, as proof of concept applications, we demonstrated that d-$Mg(OH)_2$ exhibited promising performance for intracellular ROS scavenging and PVC thermal stabilization. This work employs a scalable and industrially viable method to develop a cost-effective antioxidant capable of

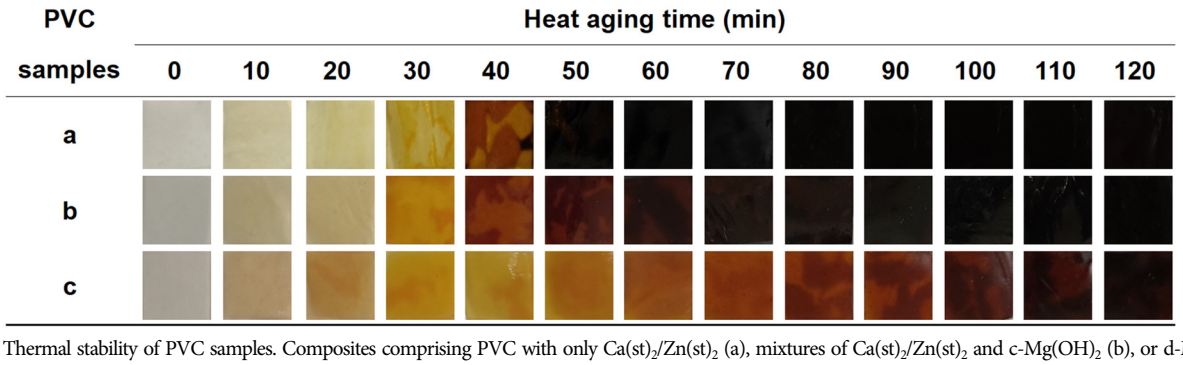

Figure 5 Thermal stability of PVC samples. Composites comprising PVC with only $Ca(st)_2$/$Zn(st)_2$ (a), mixtures of $Ca(st)_2$/$Zn(st)_2$ and c-$Mg(OH)_2$ (b), or d-$Mg(OH)_2$ (c) as heat stabilizers.

scavenging multiple free radicals, thus expanding the application avenues of hydroxides.

Electronic Supplementary Material: Supplementary material (TEM images, AFM images, XPS spectra, EPR spectra, ICP results, XAFS spectra with corresponding fitting results, and DFT calculations) is available in the online version of this article at https://doi.org/10.26599/NR.2026.94908409.

Data availability

All data needed to support the conclusions in the paper are presented in the manuscript and the Electronic Supplementary Material. Additional data related to this paper may be requested from the corresponding author upon request.

Acknowledgements

This research was supported by the Transformation of Scientific and Technological Achievements in Qinghai Province (No. 2024-HZ-805) and the National Natural Science Foundation of China (Nos. 21975013 and 22288102). This work is supported by the Innovation Fund of SINOPEC Catalyst Co., Ltd-State Key Laboratory of Chemical Resource Engineering (No. 36100000-22-ZC0607-0041). The study was also supported by the High-Performance Computing Platform of Beijing University of Chemical Technology. The authors thank the 4B7B station in Beijing Synchrotron Radiation Facility (BSRF) and beamline BL12B of the National Synchrotron Radiation Laboratory (NSRL) in Hefei for XAS measurement.

Declaration of competing interest

The authors declare that they have no known competing financial interests or personal relationships that could have appeared to influence the work reported in this paper.

Author contribution statement

J. F. L., Y. J. L., and X. D. conceived the project. J. F. L. and A. J. H. supervised the project. Z. Y. L., X. Y., X. L. Z., and Y. P. N. designed the experiments and analyzed the data. X. Y. performed the DFT calculations. Z. Y. L., X. Y., X. L. Z., Y. P. N., B. Q. W., A. J. H, and J. F. L. prepared the manuscript. All the authors discussed the results and assisted during the manuscript preparation.

Use of AI statement

None.

References

[1] Winterbourn, C. C. Reconciling the chemistry and biology of reactive oxygen species. *Nat. Chem. Biol.* **2008**, *4*, 278–286.

[2] Cao, F. J.; Feng, H.; Yao, J. X.; Hou, X.; Jin, T. Z.; Hui, J. F. Rapid synthesis of oxygen-defected molybdenum oxides quantum dots as efficient nanozymes for healing diabetic ulcers. *Nano Res.* **2024**, *17*, 6376–6385.

[3] Finley, J. W.; Kong, A. N.; Hintze, K. J.; Jeffery, E. H.; Ji, L. L.; Lei, X. G. Antioxidants in foods: State of the science important to the food industry. *J. Agric. Food Chem.* **2011**, *59*, 6837–6846.

[4] Qiu, Y.; Zhang, T.; Zhang, P. Fate and environmental behaviors of microplastics through the lens of free radical. *J. Hazard. Mater.* **2023**, *453*, 131401.

[5] Ma, H. N.; Lu, C. X.; Jin, Z. Y.; Liu, R.; Miao, Z. H.; Zha, Z.; Tao, Z. C. Rhodium-rhenium alloy nanozymes for non-inflammatory photothermal therapy. *ACS Appl. Mater. Interfaces* **2024**, *16*, 21653–21664.

[6] Scott, G. Initiation processes in polymer degradation. *Polym. Degrad. Stab.* **1995**, *48*, 315–324.

[7] Bacaloglu, R.; Fisch, M. Degradation and stabilization of poly (vinyl chloride). V. Reaction mechanism of poly(vinyl chloride) degradation. *Polym. Degrad. Stab.* **1995**, *47*, 33–57.

[8] Xue, H. J.; Zhang, M.; Li, Y. Q.; Liu, C. R.; Ma, X. Y.; He, Q. B.; Wang, Y. C.; Chen, J. X.; Qiu, J. F. Single-atom rhodium mimicking the oxidase and peroxidase for NADH cascade oxidation. *Rare Met.* **2025**, *44*, 4025–4037.

[9] Khalil, I.; Yehye, W. A.; Etxeberria, A. E.; Alhadi, A. A.; Dezfooli, S. M.; Julkapli, N. B. M.; Basirun, W. J.; Seyfoddin, A. Nanoantioxidants: Recent trends in antioxidant delivery applications. *Antioxidants* **2020**, *9*, 24.

[10] Wang, B. Q.; Fang, Y. Y.; Han, X.; Jiang, R. T.; Zhao, L.; Yang, X.; Jin, J.; Han, A. J.; Liu, J. F. Atomization-induced high intrinsic activity of a biocompatible MgAl-LDH supported Ru single-atom nanozyme for efficient radicals scavenging. *Angew. Chem., Int. Ed.* **2023**, *62*, e202307133.

[11] Wang, B. Q.; Yang, X.; Fang, Y. Y.; Zhou, X. L.; Jiang, R. T.; Han, X.; Wang, S. J.; Lin, Y. J.; Liu, J. F.; Duan, X. Amorphization activates biocompatible MgAl-layered double hydroxide for efficient multiple free radical scavenging. *Adv. Funct. Mater.* **2024**, *34*, 2404828.

[12] Liu, D. W.; Zhang, T. Y.; Gu, X. J.; Yang, X.; Han, A. J.; Liu, J. F. Layered double hydroxides supported noble-metal single-atom catalysts: Precise synthesis, microenvironment regulation, and diverse applications. *Microstructures* **2025**, *5*, 2025023.

[13] Bedair, T. M.; Heo, Y.; Ryu, J.; Bedair, H. M.; Park, W.; Han, D. K. Biocompatible and functional inorganic magnesium ceramic particles for biomedical applications. *Biomater. Sci.* **2021**, *9*, 1903–1923.

[14] Lih, E.; Kum, C. H.; Park, W.; Chun, S. Y.; Cho, Y.; Joung, Y. K.; Park, K. S.; Hong, Y. J.; Ahn, D. J.; Kim, B. S. et al. Modified magnesium hydroxide nanoparticles inhibit the inflammatory response to biodegradable poly(lactide-*co*-glycolide) implants. *ACS Nano* **2018**, *12*, 6917–6925.

[15] Cen, X. T.; Duan, H. R.; Hu, Z. T.; Huang, X.; Li, J. Y.; Yuan, Z. G.; Zheng, M. Multifaceted benefits of magnesium hydroxide dosing in sewer systems: Impacts on downstream wastewater treatment processes. *Water Res.* **2023**, *247*, 120788.

[16] Xu, S. Y.; Han, Y.; Zhou, C.; Li, J. X.; Shen, L. G.; Lin, H. J. A biobased flame retardant towards improvement of flame retardancy and mechanical property of ethylene vinyl acetate. *Chin. Chem. Lett.* **2023**, *34*, 107202.

[17] Ning, Y. P.; Sun, Y.; Yang, X.; Li, Y. P.; Han, A. J.; Wang, B. Q.; Liu, J. F. Defect-rich CoFe-layered double hydroxides as superior peroxidase-like nanozymes for the detection of ascorbic acid. *ACS Appl. Mater. Interfaces* **2023**, *15*, 26263–26272.

[18] Hennessey, M.; Whitefield, B.; Singh, P.; Alijani, H.; Abe, H.; Ohshima, T.; Gavin, C.; Broadway, D. A.; Toth, M.; Tetienne, J. P. et al. Engineering boron vacancy defects in boron nitride nanotubes. *ACS Appl. Mater. Interfaces* **2024**, *16*, 57552–57557.

[19] Xie, C.; Yan, D. F.; Chen, W.; Zou, Y. Q.; Chen, R.; Zang, S. Q.; Wang, Y. Y.; Yao, X. D.; Wang, S. Y. Insight into the design of defect electrocatalysts: From electronic structure to adsorption energy. *Mater. Today* **2019**, *31*, 47–68.

[20] Jin, J.; Han, X.; Fang, Y. Y.; Zhang, Z. D.; Li, Y. P.; Zhang, T. Y.; Han, A. J.; Liu, J. F. Microenvironment engineering of Ru single-atom catalysts by regulating the cation vacancies in NiFe-layered double hydroxides. *Adv. Funct. Mater.* **2022**, *32*, 2109218.

[21] Wen, L. C.; Guan, L.; Zhang, J. X.; Zhu, Y. J.; Chen, P.; Suo, J. L.; Zhao, B.; Zhang, R. Defect engineering boosts microwave absorption in $Ta_xNb_{1-x}C$ nanowires. *Rare Met.* **2025**, *44*, 2577–2588.

[22] Wang, X. B.; Qian, J.; Lu, Z. X.; Huang, J.; Zheng, L. R.; Jiang, Y.; Cai, M. D.; Wei, Y. X.; Guo, L. S.; Sun, S. Nitrogen-functionalized modulation of iron nanoparticles promotes selective hydrogenation of carbon dioxide. *Green Carbon* **2025**, *3*, 36–43.

[23] Yang, M. S.; Wei, T. R.; Zeng, C. H.; Zhang, J. W.; Liu, Y. F.; Luo, J.; Hu, G. Z.; Liu, X. J. CoNiOOH nanosheets array enables highly effective value-added chemicals production via nitrite and sulfide electrolysis. *Chem. Eng. J.* **2024**, *498*, 155799.

[24] Ding, J. Y.; Peng, Z. M.; Wang, Z. W.; Zeng, C. H.; Feng, Y. H.; Yang, M. S.; Hu, G.; Luo, J.; Liu, X. J. Phosphorus-tungsten dual-doping boosts acidic overall seawater splitting performance over RuO_x nanocrystals. *J. Mater. Chem. A* **2024**, *12*, 28023–28031.

[25] Ou, X. W.; Liu, X. M.; Liu, W. Z.; Rong, W. C.; Li, J. Y.; Lin, Z. Surface defects enhance the adsorption affinity and selectivity of $Mg(OH)_2$ towards As(V) and Cr(VI) oxyanions: A combined theoretical and experimental study. *Environ. Sci. Nano* **2018**, *5*, 2570–2578.

[26] Jia, C. Y.; Fan, W. L. A theoretical study of O_2 activation by the Au_7-cluster on $Mg(OH)_2$: Roles of surface hydroxyls and hydroxyl defects. *Phys. Chem. Chem. Phys.* **2015**, *17*, 30736–30743.

[27] Ma, Y.; Zhang, B. T.; Zhao, L. X.; Guo, G. S.; Lin, J. M. Study on the generation mechanism of reactive oxygen species on calcium peroxide by chemiluminescence and UV–visible spectra. *Luminescence* **2007**, *22*, 575–580.

[28] Yang, Y.; Wang, Q. Q.; Aleisa, R.; Zhao, T. T.; Ma, S. C.; Zhang, G. X.; Yao, T. J.; Yin, Y. D. MoS_2/FeS nanocomposite catalyst for efficient Fenton reaction. *ACS Appl. Mater. Interfaces* **2021**, *13*, 51829–51838.

[29] Zhang, Y. M.; Zhang, N. S.; Wang, T. T.; Huang, H. T.; Chen, Y.; Li, Z. S.; Zou, Z. G. Heterogeneous degradation of organic contaminants in the photo-Fenton reaction employing pure cubic β-Fe_2O_3. *Appl. Catal. B: Environ.* **2019**, *245*, 410–419.

[30] Foti, M. C. Use and abuse of the DPPH· radical. *J. Agric. Food Chem.* **2015**, *63*, 8765–8776.

[31] Yan, Z.; Dai, Z. R.; Zheng, W. X.; Lei, Z. C.; Qiu, J. W.; Kuang, W. J.; Huang, W. J.; Feng, C. H. Facile ammonium oxidation to nitrogen gas in acid wastewater by *in situ* photogenerated chlorine radicals. *Water Res.* **2021**, *205*, 117678.

[32] Song, R. X.; Wang, H.; Zhang, M.; Liu, Y. Y.; Meng, X. F.; Zhai, S. J.; Wang, C. C.; Gong, T.; Wu, Y. L.; Jiang, X. W. et al. Near-infrared light-triggered chlorine radical (·Cl) stress for cancer therapy. *Angew. Chem., Int. Ed.* **2020**, *59*, 21032–21040.

[33] Wei, X. X.; Wen, X. J.; Liu, Y. Y.; Chen, C.; Xie, C.; Wang, D. D.; Qiu, M. Y.; He, N. H.; Zhou, P.; Chen, W. et al. Oxygen vacancy-mediated selective C–N coupling toward electrocatalytic urea synthesis. *J. Am. Chem. Soc.* **2022**, *144*, 11530–11535.

[34] Ji, J. H.; Yan, Q. Y.; Yin, P. C.; Mine, S.; Matsuoka, M.; Xing, M. Y. Defects on CoS_{2-x}: Tuning redox reactions for sustainable degradation of organic pollutants. *Angew. Chem., Int. Ed.* **2021**, *60*, 2903–2908.

[35] Wang, B. Q.; Han, X.; Guo, C.; Jing, J.; Yang, C.; Li, Y. P.; Han, A. J.; Wang, D. S.; Liu, J. F. Structure inheritance strategy from MOF to edge-enriched NiFe-LDH array for enhanced oxygen evolution reaction. *Appl. Catal. B: Environ.* **2021**, *298*, 120580.

[36] Cheng, Q.; Huang, M.; Xiao, L.; Mou, S. Y.; Zhao, X. L.; Xie, Y. Q.; Jiang, G. D.; Jiang, X. Y.; Dong, F. Unraveling the influence of oxygen vacancy concentration on electrocatalytic CO_2 reduction to formate over indium oxide catalysts. *ACS Catal.* **2023**, *13*, 4021–4029.

[37] Liu, R. H.; Fu, S. Y.; Zhan, H. Y.; Lucia, L. A. General spectroscopic protocol to obtain the concentration of the superoxide anion radical. *Ind. Eng. Chem. Res.* **2009**, *48*, 9331–9334.

[38] Michalski, R.; Smulik-Izydorczyk, R.; Pięta, J.; Rola, M.; Artelska, A.; Pierzchała, K.; Zielonka, J.; Kalyanaraman, B.; Sikora, A. B. The chemistry of HNO: Mechanisms and reaction kinetics. *Front. Chem.* **2022**, *10*, 930657.

[39] Feng, B.; Jing, Y. X.; Liu, X. H.; Guo, Y.; Wang, Y. Q. Waste PVC upcycling: Transferring unmanageable Cl species into value-added Cl-containing chemicals. *Appl. Catal. B: Environ.* **2023**, *331*, 122671.